Fabrication of 500 MeV Superconducting Coil*

H. Blosser, N. Bird, D. Cole, B. Deimling,
C. Herrlander, and D. Lawton

Winding of the superconducting coil began in late October (1976) and was completed in late January (1977). The start of winding was delayed relative to the expected schedule as the result of vendor overrun in the fabrication of the stainless steel coil bobbin, and the winding operation took longer than expected due to unanticipated problems with manufacturing defects in the conductor. The total operation was nevertheless quite successful; we are pleased with the final coil which appears to be an unusually tight, well-insulated winding.

The basic structure of the coil consists of a layer type winding on a stainless steel bobbin. (The bobbin is afterward welded shut to become the helium can.) Major features of the coil design were described in last year's annual report. The insulation system used on the bobbin can be seen in Fig. 1. The inner bore of the bobbin is covered with two layers of 5 mil mylar, followed by a first "picket-fence" layer of 40 mil thick strips of a fiberglass laminate (NEMA G-10), the spaces between pickets forming the passages for liquid helium circulation in the coil. (In the figure, the picket fence is temporarily held in place with masking tape.) At each end of the bobbin there is a grooved endplate, also of G-10 (the middle region of Fig. 1) with alternating wide grooves which are helium feed passages and narrow grooves which position the picket fence strips by meshing with tabs on the pickets. Coil leads also feed in through these G-10 endplates, the lead to the inner layer involving two 90^{o} bends which turn the lead back on itself, and the outer lead consisting of opposite, 45^{o}, bends as can be seen in the figure. In the lead region, the conductor is doubled by soft soldering a short length of extra conductor on the side of the actual coil cable to make an approximately square conductor.

Figure 2 is an overall photograph of the winding machine, which shows the coil when winding was nearly completed. The basic component of the winding machine was a large 96" vertical lathe obtained from federal surplus. The table of this lathe is seen at the bottom of Fig. 2. The conductor appears in the figure as a fine line feeding in from the left, passing first through straightening rolls, then through a dimension-checking system, then through the tensioning system (located just behind the vertical 2x4 in the figure), then on to an insulation system in the region of the four circular reels in the figure, and finally through a presser arm and onto the coil. All of this equipment is mounted on one of the tool holders of the lathe, and the lathe feed is used to move the entire apparatus up and down as the winding layer advances. The winding system is mostly automatic, although an operator observed at all times. At each end of the layer, substantial handwork was involved both in placing the last turns and in fitting the transition blocks which carried the conductor up to the next layer.

The insulation system is as described in last year's annual report, i.e. strips of 2 mil thick mylar, creased to form a U-shaped cap which just fitted on the narrow side of the conductor, leaving the broad face of the conductor approximately 50% bare and in direct contact with the helium bath. A double sticky tape was used under the mylar on both top and bottom of the wire to hold the "U" in place. In Fig. 2, the two white round reels slightly to the left of center and above and below the conductor are the double sticky tape. The pair of close-together reels slightly to the right of center in Fig. 2 contain the 2 mil mylar which feeds into a heated creasing die, not discernible in the figure.

A number of splices were necessary in each coil; an idea of the splicing technique can be obtained from Fig. 3 which shows two pieces of conductor in the process of being spliced. The structure of the conductor, as described last year, consists of an array of 13 wires, three containing NbTi and ten consisting entirely of copper spirally wrapped about a rectangular copper coil. In making a splice, the wires containing superconductor were identified and marked (the dark wires in Fig. 2). The wires were then peeled back from the core for a length of 4", and the core was shortened by 2" on each end and joined with a scarf-type hard solder joint. The six superconducting wires were then rewrapped around the coil with an overlap region such that approximately 4" of the resulting cable contained six superconducting strands laying side by side in pairs. The remaining seven positions in the splice region were filled with copper strands, a total of 4" of length being removed from each strand in a staggered way so that joints in the strands did not line up in the conductor. The whole array was then judiciously soldered and squeezed in an alternating way until the cable reached more or less normal size. Measurements on several trial joints gave excellent results, pull tests indicating mechanical breaking strengths of approximately 90% of the unspliced conductor, and electrical resistance measurements indicating a resistance of about 1.5 nano-ohms (at $4.2^{o}K$). The mechanical dimensions of the joints were always slightly larger than the unspliced conductor (about 5 mils in each coordinate) but sufficiently similar so that no special pockets in the coil insulation were required.

At the end of every winding layer an insulation test was performed as shown in Fig. 5. The test consisted of applying full operating voltage (20 V) to the coil, and then stepping across the exposed bare section of successive turns with the leads of a milli-voltmeter which then read turn-by-turn the voltage drop in the turn. This test was both simple and effective. A change of a few percent in the resistance of a turn could be observed, and several variations of this magnitude were attributed to slight changes in the manufacturing pattern of the cable. One turn out of 6688 showed a real short (at the transition point from one layer to the next) which was easily repaired. On the basis of this turn-by-turn test, the internal insulation system of the coil is believed to be in excellent condition.

The winding tension in the coil was controlled by a servo-driven system which is shown in Fig. 6. In this figure the conductor enters at the top and passes between a pair of rubber "V" belts which are held tightly against the conductor by two sets of roller bearings, the press of the bearings being sufficient to keep the conductor from sliding relative to the belts. A hydraulic motor (seen near the top of Fig. 6) drives the two belts through gearing and pulleys in a way which causes the whole tensioning sled to maintain a pull of preset magnitude relative to a set of constant torque springs, the whole sled moving on a set of linear bearings, the ends of which can just be seen near the bottom of the figure. As the winding machine (the lathe) starts up, the conductor, held tightly between the two belts, at first tends to pull the tensioning sled forward, but the servo then immediately reacts through the hydraulic motor, and drives the belts at a speed to maintain the sled in constant position. This corresponds to constant pull by the springs and therefore a constant winding tension. Using this system, the conductor was wound with the design tension of 2000 psi maintained to an accuracy of ±10%. A similar but different servo system was used to provide the much higher tensioning, namely 20,000 psi, in the aluminum banding on the outside of the coil.

Figure 4 is a view of the completed coil with the outer stainless steel wall of the helium can already in place on the lower half of the coil, and with the aluminum banding and coil leads clearly visible in the upper half of the figure. The median plane structure involves removable stainless steel slabs (the IBM card carrying the numeral 6 being attached to one of these removable slabs by a piece of masking tape in the figure). Each of the three 120° sectors consists of three of these removable 35° stainless steel slabs, plus one 15° welded-in-place slab. One of the 15° slabs is visible just at the left of the numbered removable slab in the figure. Symmetric pairs of coils are internally tied in series within the cryostat in order to avoid any possibility of breaking the median plane symmetry with some accidental external short. In the figure, the two leads to the mirror image large coil pass through the median plane in the fixed 15° block at the lower left of the figure. At the upper right the leads pass into the upper helium header, and eventually to bus bars going to the external leads. Also at the upper right, the two leads from the small coil pair can be seen entering from the right-hand edge of the figure. (The vertical rod just at the region where the left and right leads join is one of the American Magnetics Helium Level Detectors.)

After the helium can was closed and vacuum tested, the entire helium vessel was hand-wrapped with ten layers of aluminized mylar plus "Dexter" paper. The entire bobbin was then dropped into an annular aluminum nitrogen shield, and this shield was further insulated with an additional 15 layers of aluminized mylar and paper. The coil with nitrogen shield and insulation is shown in Fig. 7 hoisted in the air for final work on insulation of the lower support link members. One of the epoxy fiberglass support links can be seen just at the left of the person in the dark shirt with back to the camera. The support links are basically as described in last year's report, and each was tested to 43,000 lbs. by lifting a deadweight load consisting of one of the outer magnet rings.

Figure 8 shows the completed coil installed in the room-temperature steel cryostat. The cryostat is also already installed in the magnet yoke in the figure, and the upper yoke slab is being lowered into place in preparation for initial tests, described in a separate section of this report (see article in this report, "Operating Experience..." by Mallory et al.).

---

*General design features of the 500 MeV cyclotron were described in last year's annual report (pp 95-111). Generally the basic design remains as described therein although with some changes as the design has been further detailed and refined through the year. The most recent published report on the cyclotron appears in the Proceedings of the Seventh International Conference on Cyclotrons and Their Applications (Birkhäuser, Basil, 1975, p 584).

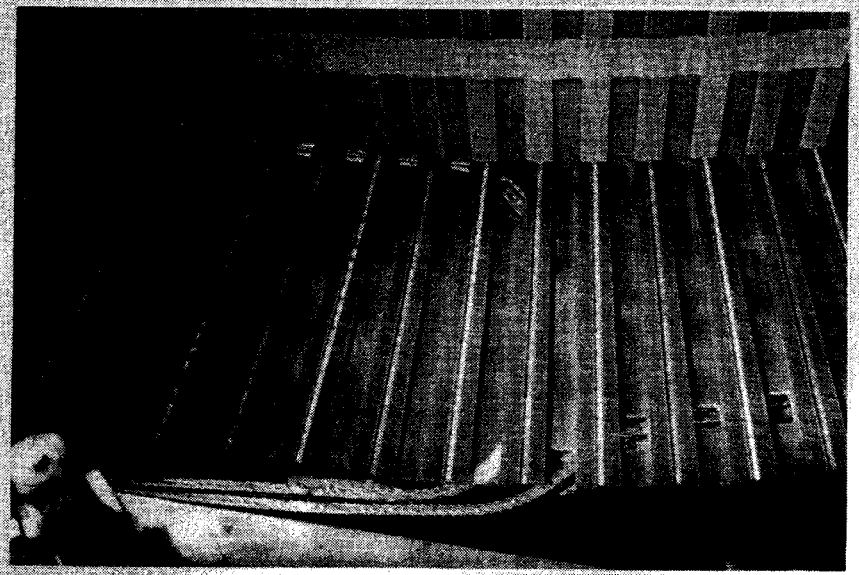

Fig. 1. View of insulation system on coil bobbin. (NOTE: The text gives expanded descriptions for all figures in this article.)

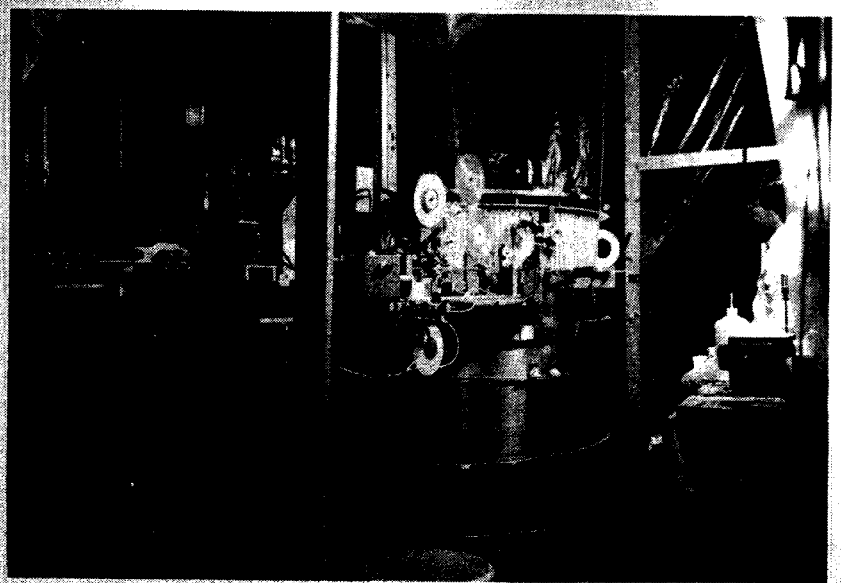

Fig. 2. Coil winding machine in operation.

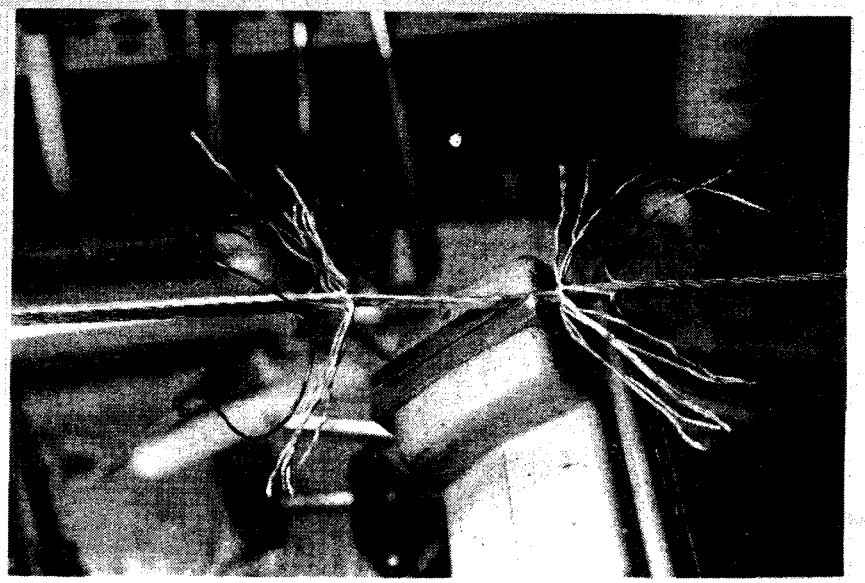

Fig. 3. Conductor splice in process.

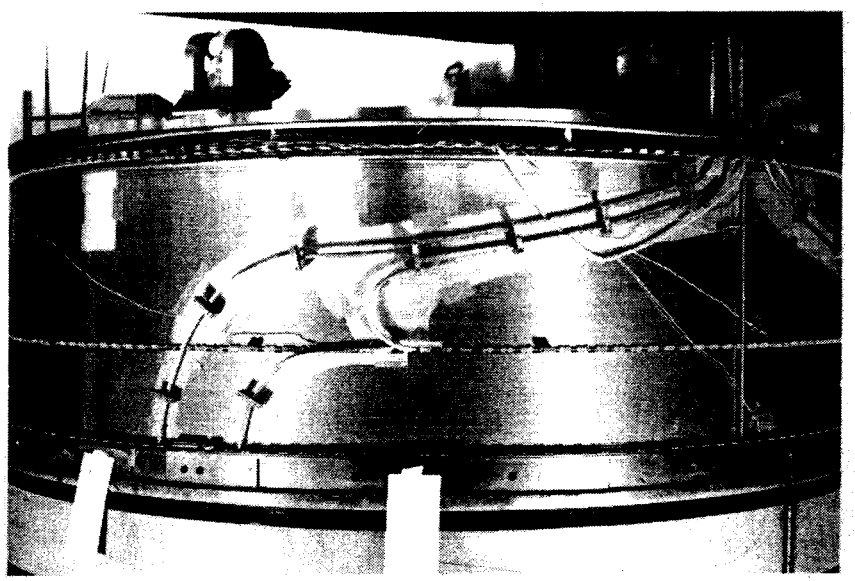

Fig. 4. View of completed coil (lower helium can cover already in place).

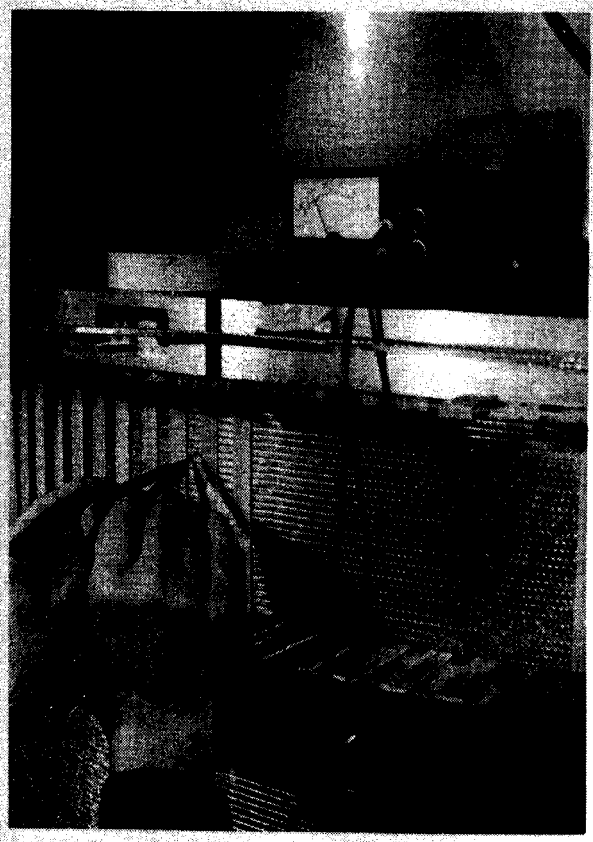

Fig. 5. Testing for turn-to-turn shorts.

Fig. 7. Coil with superinsulation.

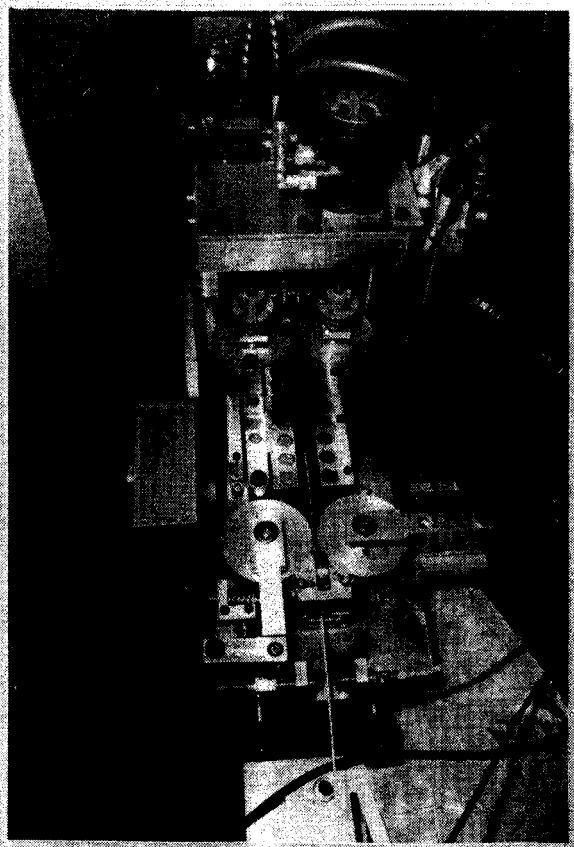

Fig. 6. Servo-controlled tensioning system.

Fig. 8. Final magnet assembly.

Instrumentation for the Main Coil of the 500 MeV Cyclotron

P. Miller, H. Blosser, D. Gossman, J.F.P. Marchand, B. Jeltema

All instrument leads that enter the helium bath are Teflon insulated #28 AWG wires made of a low conductivity alloy, either Tophel or Cupron, supplied by Magnet Wire Supply Co., Chatsworth, California. Insulation was tested at 5kVDC to a ground plane and wire-to-wire in a twisted pair without breakdown occurring. A total of 104 leads come out of the cryostat to three connectors located at the refrigeration port (Table I).

Table I.

Name	Connector Description	Devices	Pins Used
1P	50 pin male	PT 1-4, HELS 1-8	42
2P	50 pin female	FSC 1-2, TC 1-9, 11-13, 19-21, SG 1-4	50
3P	15 pin	TC 10, 14-18	12

The wires for each connector were pulled through a .38" dia. stainless steel tube which was plugged with epoxy at the outside surface. The Teflon insulation was treated with Tetra-Etch to allow the epoxy to bond to it. We found that the large bundles of wires should not be twisted, as that increases the overall diameter. With such a tight fit, the insulation can be damaged as the bundles are pulled. The heat leak due to thermal conduction along a wire without any gas flow for cooling is calculated to be $P=8.4 \times 10^{-4}$ watts/wire. The power carried to the helium bath by all 104 leads is about .09 watts. A diagram showing the sensor locations and the wire routes appears in Fig. 1.

Coil and Lead Voltage Monitors

A sensitive voltmeter was connected between the center tap of each coil and a resistive divider connected across the coil ends (bridge circuit) to measure any asymmetry in the coil voltage distribution with respect to the midplane of the magnet. No significant imbalance signals were seen.

A voltage drop across each of the four vapor cooled current leads was monitored. One lead failed to reach equilibrium at 700 A. When its voltage drop reached 200 mV the current was ramped down. The gas flowmeters were checked and found to be reading correctly and indicating sufficient flow for cooling of the lead. In a subsequent run at 600 A the lead seemed stable, and the voltage drop was below 100 mV. All leads gave a voltage drop of about 100 mV at 700 A in the test dewar before assembly in the magnet. We plan to monitor these voltages closely during future testing at high current. The leads were manufactured by American Magnetics, Inc., Oak Ridge, Tennessee.

Platinum Thermometers (PT1-4)

Four sensors were intended, but only three are installed in the coil, due to breakage of one sensor (PT3) at the last minute. It is replaced by a thermocouple (TC20). They can be read individually on a single readout unit equipped with a sensor selecting switch. The sensors and readout unit come from American Magnetics, Inc. These devices worked perfectly and are very convenient to use. Their main drawback is high cost ($70/sensor).

The platinum sensors are arranged in pairs to measure the average radial temperature gradient across the coil. They are installed in holes in the G-10 spacer ring between the large and small coil. PT1 and 2 are in the lower half of the magnet, and TC20 and PT4 serve the same purpose in the top spacer (roughly 180° away). Typical temperature difference during cooldown across the 6 1/2 inch radial distance was 10 K.

Thermocouples (TC1-21)

All thermocouples consist of Tophel-Cupron junctions, soldered with special solder containing antimony (63% Sn, 36.65% Pb, .35% Sb), part no. 361A-20R, Micro-Measurements, Inc., Romulus, Mich. Voltage center taps (TC10, TC18) were soldered to the coil with 50-50 Sn-Pb solder, (used to manufacture and splice the superconducting cable). Voltage taps to the coil leads (TC14-17) are soldered to a ground lug (with 361A-20R) which is held by the clamping screw at the junction of the superconducting bus bar and the cold end of the vapor cooled current lead.

The reference junction is inserted into a liquid nitrogen dewar outside the magnet yoke. Its wires run to the thermocouple connector P2 in order to minimize temperature differences among its connections and those of the other thermocouples in the coil.

We measured a temperature calibration for the thermocouples, shown in Fig. 2. For temperatures from 77 K to 4.2 K the standard was a factory-calibrated platinum thermometer which was compared with a copper-constantan thermocouple and found to agree. A probe assembly carrying the sensors was attached to the end of a stainless steel tube and inserted to various depths into the cold helium gas in the 500 liter dewar and allowed to reach equilibrium. The copper-constantan thermocouple alone was the standard for calibration at higher temperatures. Some data furnished in the manufacturer's catalog appear in Table II.

The thermocouples are connected to the computer-controlled digital voltmeter (Hewlett Packard 3490 A) through the reed relay multiplexer (Matrix Corp. 1701), which is the same apparatus

used to map the magnetic field in conjunction with an array of flip coils and integrators. A computer program reads the thermocouple voltages on demand, converts them to Kelvins and prints them in an array which represents the position of each sensor in the coil (Fig. 3).

Table II.

Alloy	Composition	Elect. resistivity @ 25°C	Thermal EMF vs. Platinum 27 0-100°C
Tophel	90% Ni, 10% Cr	68.0 μΩ-cm	+.024 mV/°C
Cupron	45% Ni, 55% Cu	48.9 μΩ-cm	-.035 mV/°C

Six of the thermocouples (TC10, TC14-18) are voltage taps not intended for temperature measurements. They are isolated in a separate connector (P3) and are not connected to the readout apparatus, although the computer program includes them in case they are needed. The others are all attached at various points to the outer surface of the aluminum banding except for the following:

TC8 - on outer wall of stainless steel helium container, near refrigerator inlet.

TC19 - inside helium gas return line to refrigerator.

TC20 - at inner wall of cryostat, replacing PT3.

TC21 - reference junction, outside magnet.

Helium Level Sensors (HELS 1-8)

The sensors and readout units were purchased from American Magnetics, Inc. There are two sizes of sensor. In the coil there are four 18-inch sensors, two of these below the median plane, about 180° apart, and two symmetrically above them. These sensors are not replaceable.

The three top ports of the cryostat contain a total of four 5-inch sensors, two in the port with coil leads, and one in each of the others. One of the two sensors in the lead port (HELS5) apparently shorted out after about one day of operation in liquid helium.

There is one readout unit for the 18-inch sensors and two for the 5-inch sensors (different calibrations). Both readout units for the 5-inch sensors have high/low set points for operating indicators or control circuits (not used until now).

Magnetic Field (dB/dt) Sensing Coils (FSC1-2)

There are two sensing coils in the magnet, one in each G-10 spacer plate separating the large coil from the small coil. The field sensing coil consists of one turn of #30 AWG teflon insulated stranded copper wire wrapped around the stainless steel bobbin. It is held in a groove machined in the edge of the G-10 spacer plate. For the initial testing of the magnet the two field sensing coils are connected in series opposing so the difference in the signals could be directly displayed on a chart recorder (1 mV span). No significant imbalance signals were observed.

Strain Gauges on Banding (SG1-4)

There are four separate strain gauge bridges installed, one for each half coil, to measure strain in the aluminum banding. In each bridge there are two active gauges on the banding and two compensation gauges on an unstrained aluminum block nearby. The gauges are type CEA-13-125-UW-350, supplied by Micro-Measurements, Inc., Romulus, Michigan, applied with AE-15 epoxy adhesive as recommended. Gauge resistance is 350 ohms. All four transducers read as full bridges, with a sensitivity factor of 2 (for 2 active gauges) and a gauge factor of 2.145 at 24°C.

These gauges have not yielded any strain measurements, except at room temperature before cooldown. The apparent strain readings change erratically and by large amounts, comparable to the strain induced by the winding tension, both during cooldown and when the coil is in liquid helium. According to the manufacturer, the temperature-induced variations are large and unpredictable, but once a liquid helium bath is established the gauge readings should be valid. A possible explanation of the observations is that the epoxy bonding agent was fractured by thermal shock, releasing a gauge from the surface.

We have analyzed the effect of temperature on the bridge wiring and find that this cannot explain the results. Tests of a sample unstrained bridge show a substantial temperature effect when the bridge is cycled to liquid nitrogen temperature, in agreement with the range of responses expected by the manufacturer.

Before the first cooldown of the coil, the strain readings on three of the gauges were measured several times over a 20-day interval as a check on stability and were found to vary slightly. No steady elongation (creep) was observed. The variations were consistent with estimates of temperature-induced differential expansion.

Strain Gauges on Coil Support Links, LG 1-9

The coil support links incorporate standard gauged threaded studs supplied by Strainset, Inc., 24 Summit Grove Ave., Bryn Mawr, Pa. 19010. The six axial links use 1-inch diameter studs rated at 45,000 lbs each; the three radial links use 5/8 in diameter studs with a 15,000 lbs rating. The load calibration in terms of strain reading was supplied by the manufacturer at full load for each stud.

If the coil is not centered in the surrounding steel, magnetic forces will appear in the links when the magnet is energized. These are minimized by a mechanical adjustment of the links. The top links were adjusted to the correct measured length before the coil was inserted in the vacuum jacket. After cooldown, the

bottom links were tightened to 3000 lbs tension in each. The axial tensions were set at 1500 lbs.

When current was applied to the magnet we found that the axial position did not require correction, but the radial links indicated an offset. After a test adjustment we observed that the coil was unstable radially, i.e. the link with the highest tension must be shortened to center the coil. Centering was accomplished easily in several iterations, and the magnetic forces in all links remained below 10% of their rated capacity at full current.

For these measurements, we used a strain indicator (type HW1-D) and a 10-channel switch and balance unit (type SB-10C) manufactured by Strainsert. The separate zero capability for each channel was not used; a four pole switch would be suitable for the present purpose. All balance controls were adjusted for absolute zero to allow monitoring long-term changes in readings (instrument can be readily reset to absolute zero at any time).

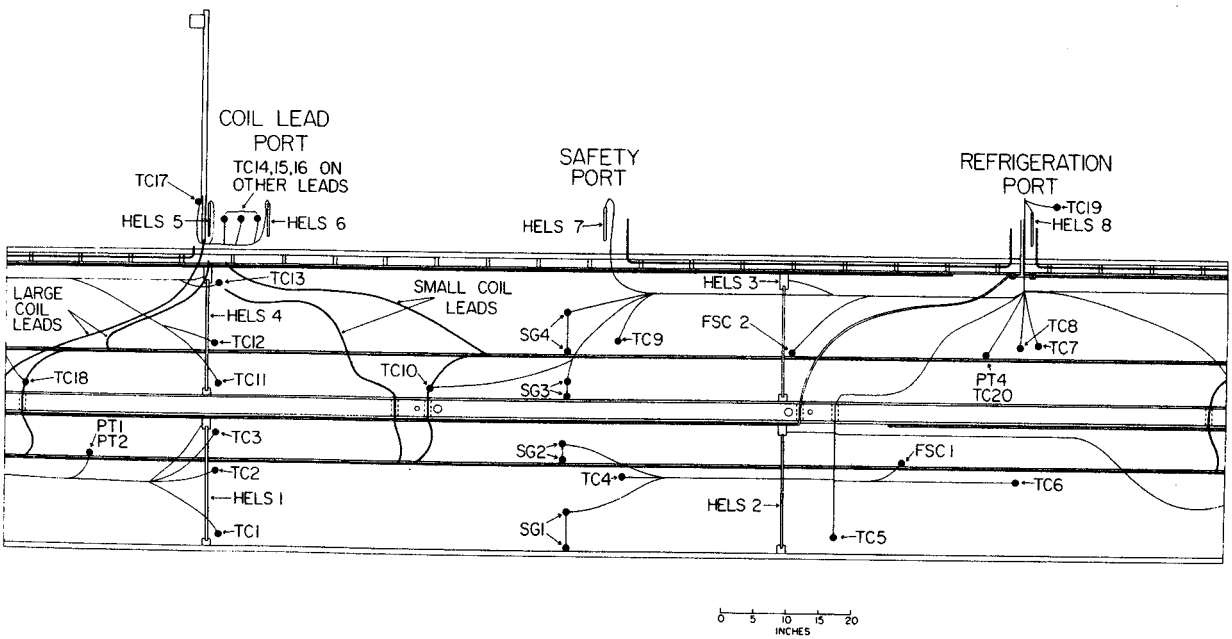

Fig. 1.--Side view of coil surface showing sensor and lead locations inside the helium chamber. This representation is as if the coil surface were unrolled, to show the entire circumference. The coil support links and their strain gauges (LG1-9) are not shown.

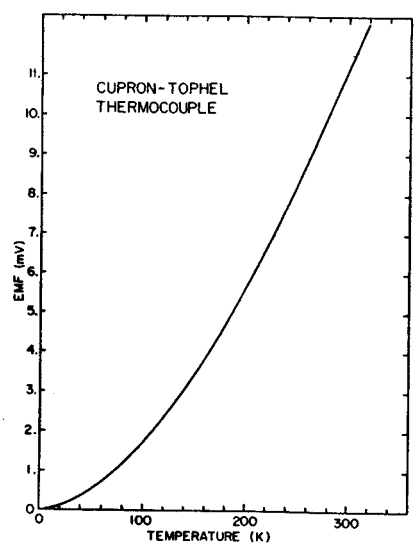

Fig. 2.--Calibration curve for Cupron-Tophel thermocouple junctions.

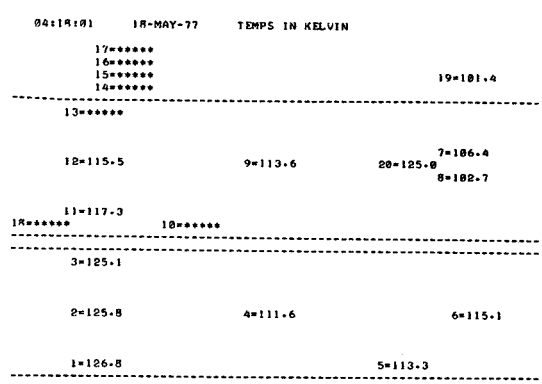

Fig. 3.--Sample output from thermocouple measurement program. The temperature readings shown are in the range 100-130 K. Thermocouple number 13 is inoperative; other thermocouples not read are attached to the coils for voltage sensing. The dashed lines represent boundaries of the upper and lower portions of the entire coil.

Magnetic Field Mapping System

P. Miller, H. Blosser, D. Gossman, B. Jeltema, and J.F.P. Marchand

This report describes the apparatus and procedures we plan to use for mapping the field of the 500 MeV magnet. The system uses 55 flip coil/integrator sets with computer controlled data scanning. The hardware is similar to that developed to map the field of the Oak Ridge cyclotron.[1]

Moving parts are mostly non-metallic to reduce eddy current effects. The coils are wound on Delrin bobbins with an outer diameter of 3/8", and contain about 560 turns of #34 AWG enamelled copper wire. They are mounted .5" apart in holes drilled in a 7/8 dia. rod made from G-10 epoxy-fiberglass material. The rod is rotated by strings connected to a non-magnetic air operated piston (see Fig. 1). The probe mechanism has to fit within the 1" magnet gap between pole liners. The azimuthal drive mechanism and the strings for rotation of the rod pass through the center hole in the magnet yoke. Electrical wires are routed through another large hole in the yoke.

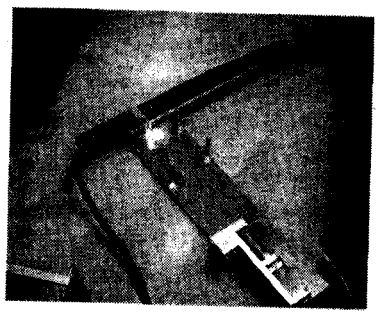

Fig.1--Probe rod and rotation mechanism configured for calibration in a uniform field magnet. The azimuthal drive is not shown.

The integrators use .022 μf, 100 V polystyrene feedback capacitors (Mallory SXM122) and 1 megohm 1% metal film input resistors (mfg. Dale). The operational amplifiers are Analog Devices type 234L. Five integrators are assembled in one NIM module. Eleven modules are therefore required. A Hewlett Packard 3490 A digital voltmeter scans through the integrators by means of a reed relay multiplexer (Matrix Corp. 1701). The measurement cycle for 55 integrators takes about 18 sec (relay setting time 100 msec plus measurement time of 230 msec per channel). The voltmeter is inherently insensitive to noise pickup at the power line frequency or its harmonics. The calibration constant for each channel was obtained by operating the apparatus in a uniform field measured with an NMR probe. Calibrations at 4 fields (1.5 to 13.5 kilogauss) confirm linearity of the response to within 1 part in 10^3, extrapolating to 60 kilogauss. The calibration constants are approximately 1.5 volt/Tesla.

The temperature coefficient of the calibration constants was determined experimentally. In the early design stages, temperature compensated ceramic capacitors seemed to be the best choice, and temperature regulation of the integrators was thought to be unnecessary. Further testing revealed that the polystyrene capacitors, having negligible leakage and smaller dielectric polarization, would be a better choice in spite of their negative temperature coefficient of about $10^{-4}/^{o}C$. We plan to add temperature control if experience shows it to be necessary. The effect of temperature changes on the integrators and on the coils themselves has been measured directly.

To allow corrections for varying drift rate, the field is measured twice at each azimuth. The cycle used for this purpose is given in Table I.

Table I. Basic Measuring Sequence.

Event	Time Required
Check DVM (optional)	3 sec.
Rotate probe arm (+180°)	3 sec.
Rotate probe arm (-180°)	3 sec.
Read integrators	18 sec.
Rotate probe arm (+180°)	3 sec.
Read integrators	18 sec.
Read integrators	18 sec.
Rotate probe arm (-180°)	3 sec.
Read integrators	18 sec.
Advance azimuth by 2°	3 sec.
**	
Repeat 180 times for complete 360° scan.	4.5 hours

The computer algorithm can use the exact time of each voltmeter reading to determine the drift rate. Initially we have used a simple average of the two sets of readings (+180° and -180°) to correct the voltage difference for each flip. The computer prints a message to alert the operator if the drift rate becomes excessive. Magnetic field values calculated through the use of a calibration table are then stored on a disc for later Fourier analysis. The full array of integrators and coils are now being tested and calibrated. Prior testing has been done with a single coil. Repeatability of the readings in a test magnet leads us to expect a precision of better than 1 part in 10^4 for measurements in one map.

The apparatus using a single coil and integrator was used successfully to measure the field of the 500 MeV magnet during its initial operation. The first mapping cycle is expected to start in October, 1977, when the pole tips are installed.

1. S.W. Mosko, E.D. Hudson, R.S. Lord, D.C. Hensley, and J.A. Biggerstaff, IEEE Transactions on Nuclear Science NS-24 (June 1977) 1269.

Operating Experience with the Helium Refrigerator-Liquefier System and the Superconducting Coil

M. Mallory, H. Blosser, P. Miller, D. Magistro, and D. Johnson

A CTI 1400 refrigerator-liquefier was acquired to provide the cooldown of the superconducting magnet and to make liquid helium. Figure 1 is a block diagram of the superconducting cyclotron helium system. The major components of the system are, 1) the magnet cryostat; 2) a 9733 gallon helium gas reservoir tank; 3) a 500ℓ liquid helium dewar; 4) a CTI 1400 refrigerator-liquefier (with dual charcoal filter traps and variable engine speed control); 5) two 55 cu ft/min helium compressors; and 6) all interconnecting liquid helium transfer lines. An existing liquid nitrogen system was used, and required construction of transfer lines to the appropriate ports. The helium system is designed to be a closed loop system.

CTI, Argonne National Laboratory, Fermi Laboratory and various individuals were consulted about cryogenics problems. In the following sections a chronological description of procedures that the helium system was subjected to during the past year is given. Details of unusual experiences are also reported, that although not totally unexpected to the cryogenic expert, were not present in our planning and we hope will be of use to other groups in the cooldown of their superconducting cyclotron magnets.

The helium refrigerator-liquefier was delivered in late July 1976. The installation and connection of the refrigerator to the 500ℓ dewar was completed by September and the system started up with the aid of CTI personnel. From September to December, liquid helium was made approximately every three weeks in quantities of 200ℓ. The major problem encountered was the loss of helium gas from the boil-off of the 500ℓ dewar during periods of refrigeration shutdown. A procedure that required modification of the control system of the refrigerator was developed. The pressure in the 500ℓ dewar was allowed to increase to 10 psi. At this pressure a valve to the pump suction is open and the helium compressor turned on. The refrigerator is left in the recovery mode with the result that the boil off gas is pumped into the reservoir tank until the dewar pressure reaches 1 psi. This system enables complete cap-

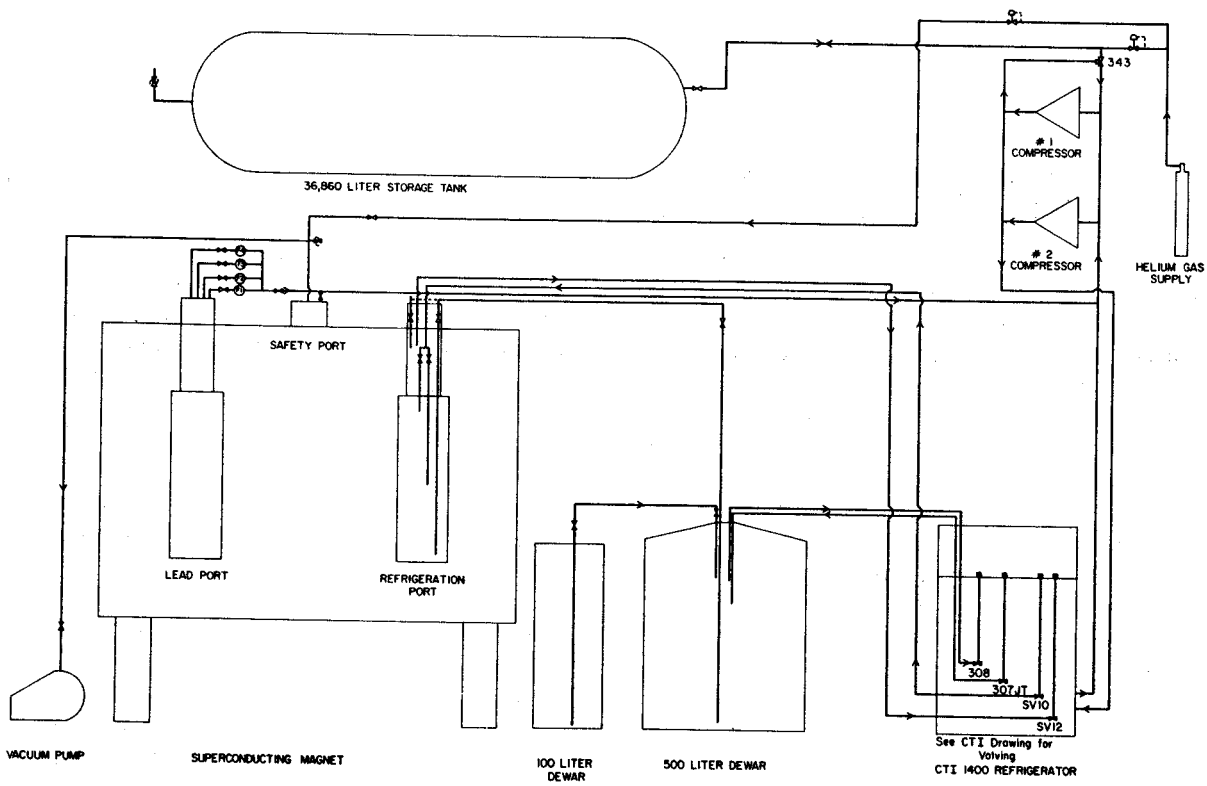

Fig. 1.--The helium system block diagram for the 500 MeV superconducting cyclotron. The system is a closed helium loop. The return cold helium gas line appears to be conductance limited and restricts our initial cooldown rate. Use of the leads return lines to the pump suctions will improve the conductance limit problem at start-up.

ture of the helium gas but does result in increased boil off of the 500ℓ dewar (~3%/day) due to a lack of shield cooling.

In January, a small test dewar was completed, where many of the construction techniques planned for the magnet cryostat were tried. This test dewar was cooled in the same manner as planned for the magnet cryostat, and was used to check the current leads of the superconducting magnet. Several problems were encountered by the test dewar. A silver solder joint was inadvertently included in the construction of the dewar and it immediately cracked upon cooldown. The importance of a safety pop-off valve on the vacuum jacket was demonstrated when the test dewar warmed up and released large quantities of gas that had been cryopumped. Initially a large vacuum leak in the valve connecting the mechanical pump to the test dewar existed and a long time passed before it was discovered. The problem of "heat pulse" (a quantity of high temperature gas being returned unexpectedly to the refrigerator) was encountered, with the consequence of pressure increase on the pump suction and venting of gas overboard. The procedure of valving the return gas to the appropriate temperature range of the refrigerator heat exchanges and restricting the supply of cold gas controlled the gas venting.

In March 1977, the magnet coil helium can was completed and it was cooled as low as possible with the refrigerator in order to stress the welds. A temperature of 240 K was reached after two days of cooling. From hindsight, a weld at the entrance of the cold helium gas into the helium coil can did crack, however our method for detecting this small helium leak was inadequate. The warm-up procedure used, namely using the recovery mode to pump the gas back into the helium gas reservoir until the magnet reached room temperature, caused contamination of our helium gas reservoir. The warm-up mode now adopted and proven successful is to disconnect the magnet cryostat from the helium system while its temperature is below 70 K. The excess helium pressure build-up, as the magnet warms, is vented overboard.

In April, the vacuum jacket was completed around the helium can and the helium leak discovered. It was decided to cool down again, in order to stress the welds as much as possible. A temperature of 180 K was achieved after 50 hrs. of cooling. The helium coil can was then removed from the vacuum jacket and the helium leak found by soap bubbles.

On May 14, cooldown was again started. Figure 2 is the temperature of the most extreme sensors in the coil as a function of time. The cooldown required approximately 130 hrs. The pressure in the magnet cryostat was between 12-15 psi. At 18 psi, a pop-off in the refrigerator causes helium to be vented. At the beginning of

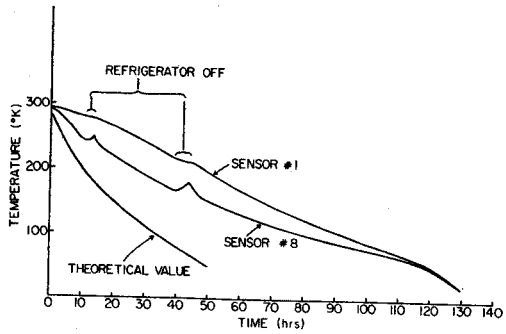

Fig. 2.--The cooling curves for the superconducting magnet is shown. Sensor #8 is located near the entrance of the cold helium gas from the refrigerator and is closely coupled to the operation of the refrigerator and does not properly reflect the temperature of the coil. Sensor #1 is located the furthest from the entrance of the cold helium gas and represents the warmest coil temperature. The theoretical minimum cooling time curve is also given and improvements in the cooldown procedure and correcting of heat leaks will allow cooldown times to approach this curve.

the cooldown, the gas flow to the magnet cryostat was approximately half of the refrigerator capacity. It appears that the helium gas return line to the refrigerator is conductance limited. In the initial cooldown phase, this conductance limit can be solved by allowing some of the gas to be returned to the pump suction through the current leads, and this will be tried next time.

At approximately 20 K the helium system was disconnected from the magnet cryostat and the magnet yoke completely assembled. The cooldown lines and the liquid helium transfer line from the 500ℓ dewar were then installed. The refrigerator was used to pressurize the 500ℓ dewar (~8 psi) and liquid helium transferred to the bottom of the coil. Initially a large heat pulse was encountered, which may in part be attributed to a hot transfer line. However as the helium level increased in the cryostat, additional heat pulses were encountered at height positions that are associated with separation baffles in the coil sections. The maximum temperature of these heat pulses was 80 K, while all temperature sensors indicated the coil was below 10 K. The heat pulses were handled by adjusting the helium transfer rate and valving the hot gas to the appropriate temperature range in the heat exchanger of the refrigerator.

When the helium level reached 60% in the upper coil chamber, the supply of helium of the 500ℓ dewar became very low and necessitated adding additional liquid helium to the system. 100ℓ of liquid helium was then added to the cryostat thru the top helium transfer line. No noticeable helium level increase occurred, and we concluded that adding liquid helium from the top of the cryostat is certainly different from adding at

the bottom. Namely, all of the heat energy must be removed from all coils before any liquid accumulation begins.

At this point it was decided to energize the small coil since it was completely covered with liquid helium, and this was successfully done up to 400 A with no noticeable consequences on the helium system.

Next, 100ℓ of liquid helium was added to the 500ℓ dewar. The entrance valve to the 500ℓ dewar required depressurization of the dewar and hence stopping the transfer to the magnet cryostat. This succeeded in increasing the inventory of liquid helium to the system and the magnet cryostat was filled above the coils to a level between sensors in the large volume reservoir which represents a dead region in the helium level detection system. The liquid helium transfer line was shifted to the top helium fill port, the helium flow rate to the magnet cryostat was adjusted to maintain a constant level of helium in the 500ℓ dewar and the system was left to run overnight. The next morning, helium was detected in the refrigeration port. The helium bleed valves in the other ports were adjusted, and a 5" difference in the helium height around the top of the cryostat could be made, even though the ports have a common pressure connection.

The magnet coils (series connected) were then energized to 400 A at a 20 volt ramp. The helium pressure increased beyond the pop off limit in the refrigerator and the gas was vented overboard. The magnet was immediately run down from 400 A, since the helium level had dropped below our sensor in the lead port. The helium level dropped to the 60% height of the top coil before the pressure surge was brought under control. It was concluded that the charging rate was too high, and eddy currents in the aluminum banding around the coils were boiling helium excessively.

The next day a ball valve was added to our 500ℓ dewar. It was charged with 100ℓ of liquid helium, which was easily transferred into the cryostat and filled all ports. The magnet was then energized at a 10 volt ramp, stopping at 200, 400, 600 and 700 A (where 700 A is the design value). The refrigerator was able to handle this charging rate. About ten minutes after charging stopped, the system was pumping additional gas from the helium reservoir. This indicated that excess refrigeration cooling capacity is going into making excess liquid helium. From the rate of gas flow, the heat load of the cryostat is estimated to be ~16 watts, where it is assumed the refrigerator is adjusted for maximum capacity. The appearance of a vacuum leak in the liquid nitrogen heat shield required all of the above operation to be without benefit of the liquid nitrogen, and the large heat load can be accounted for by this loss.

The magnetic field outside the yoke was measured in the median plane with a rotating coil gaussmeter. These data appear in Fig. 3. The external field is expected to be several times larger near holes through the yoke and near the magnet axis.

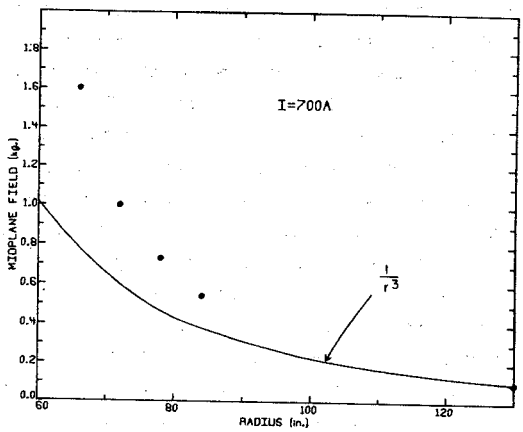

Fig. 3.--Radial distribution of the external field in the median plane at maximum full excitation. The outer edge of the yoke is at a radius of 60 inches. The motor in the gaussmeter would not operate when the probe was closer than R=66 inches (magnetic field effect). A $1/r^3$ curve has been plotted for reference.

The magnet was ramped down to 350 A and the dump circuit triggered. This caused the pressure to increase and helium vented overboard. The system recovered in ~1 hour and was ready to go again. The next day the magnet was charged to 600 A and run at that current for three hours. During this time, the radial profile of the magnetic field at one azimuth was measured with a single flip coil inserted through one of the median plane holes in the yoke. These data, and the calculated field profile are shown in Fig. 4.

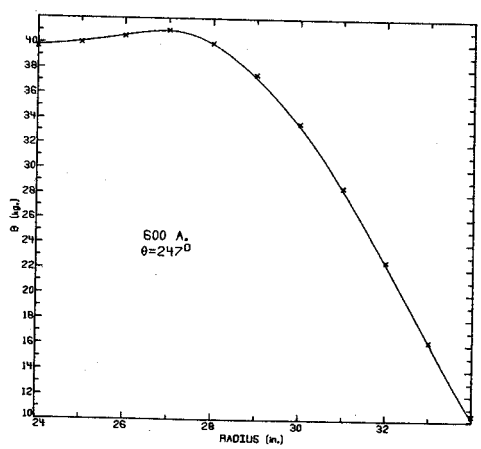

Fig. 4.--Radial magnetic profile measured (x) and calculated (curve) for a current of 600 A in the coil. The rms deviation is 0.19 kg, or roughly 0.5%.

The excellent agreement, even in absolute magnitude, between the calculation and the measurement further confirms the expectation that such superconducting magnets can be designed without the traditional approach through scale models.

The next objective was to dump the magnet and observe the response of the refrigerator and the electrical parameters. We estimated that about 15,300 joules would be dissipated by eddy currents in the aluminum banding by the dump. This energy would boil 6 liters of liquid helium at 4.2 K.

When the dump was triggered there was some venting of gas while the cryostat remained connected to the refrigerator. The cryostat return cold gas valve was closed after three minutes, with the result that the cryostat pressure increased from 2 psi to 6 psi, but this stopped the venting of gas from the system. The heat energy acquired during dumping was then extracted at the maximum capacity of the refrigerator, and the helium system was ready to go the next day. It was then found that the engine speed of the refrigerator could be easily adjusted to match the heat load of the magnet and maintain a constant helium level without using make-up gas from the helium reservoir.

The voltage across the large coil (roughly 2/3 of the whole) and the current were monitored during the dump. Their decay curves appear in Fig. 5. The total inductance can be inferred from the decay rate and the known external resistance. At 600 A, the inductance of the whole coil was about 55 H, while at 100 A, it had increased to about 100 H. This behavior had been predicted by the relaxation code TRIM used in the design of the magnet.

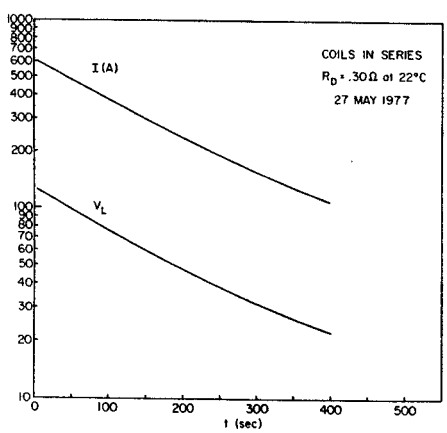

Fig. 5.--Decay curves for dump with series-connected coils from 600 A. The resistance of the dump resistor is estimated to be 0.36 Ω after the dump, from the rise of the water bath temperature.

On May 30 a minor failure occurred in one of the helium compressors, causing a loss of 200ℓ of liquid from the cryostat before being discovered, and it was decided to warm the cryostat. The magnet cryostat was disconnected from the helium system at 70 K and the vacuum jacket raised to 100 microns at 100 K with nitrogen gas. The coil warming rate from 100 K to room temperature was ~20 K/day. A small pressure surge in the helium coil can was noticed at ~260 K.

In general, we conclude that our helium system is designed adequately to handle all needs of our superconducting magnet and that the methods and skills required to run a low temperature helium system are now in hand.

R.F. System

J. Riedel

The conceptual design of the rf system is now complete and detailed drawings of the rf structures and detailed design and development of the electronics are underway. Computer calculations, and work on a small rf model have convinced us that we can successfully excite the dees on the fundamental frequency, which requires three independent rf systems working 120° apart in phase. This permits us to reduce the required frequency range, which now is from 18 to 60 Mhz. The peak rf voltage is still 100 KV and the minimum gap transverse to the magnetic field is 1 cm. Parallel to the field, the gaps will be larger than 3 cm.

R.F. Structures

Each dee will be supported by two vertical 4" diam. stems, on top and bottom, which are concentric with 9" diam. outer conductors situated in each of 6-10" diam. holes which penetrate the 30 cm of magnet iron. Gross tuning will be accomplished by moveable shorts between inner and outer conductors, the travel for these shorts being from 1 ft. to 10 ft. from the median plane. Instead of using pushrods to move these shorts, we choose to have the shorts "walk" using hydraulic actuators. These actuators and a certain minimum space below them to accommodate the coiled-up flexible water and hydraulic pipes require another 5 ft., so that the total length of each stem is 15 ft.

The center of the stems is used to accommodate the water pipes for dee cooling, and in the bottom three stems, the cryogenic lines to the cryostat vacuum pumps mounted within each lower dee half. The sliding short circuits will only be moved with rf off, fine tuning being accomplished with 1±.5pf hydraulically actuated bellows type capacitors mounted above and below each dee permitting ±.1% $\Delta F/F$ control.

Each dee will be driven by a 50Ω transmission line mounted in each of 3-3" diameter holes which penetrate the magnet iron and capacitively couple to the dees. This capacitor must be varied from 1 to 4 pf's over the frequency range, but ±20% accuracy of setting is adequate. To measure the phase difference across this capacitor, and to measure the dee voltage and a possible voltage difference (due to nonsymmetric adjustment of the stem shorts) from top to bottom of each dee, three coax monitoring cables per dee will have to be brought out through the vacuum.

Figure 1 is a schematic drawing of the equivalent rf structures, including the final transmitter. Table I shows various parameters for the frequency extremes.

Although the mechanical design of the rf structures is very complicated, and the assembly and disassembly almost impossible, we have very ingenious mechanical people who no doubt will come up with satisfactory detailed designs for all these. However a possible problem area arises from the large rf currents flowing across the stem sliding shorts. The linear current density of 70 amps per centimeter at 60 mHz is a factor of two larger than anyone else, to our knowledge, has ever successfully achieved with sliding finger stock contacts. Therefore, we have made some tests in vacuum at 21 mHz to determine what the current capacity of contact fingers is. The results were that copper on copper was good for only 5 amps per contact whereas silver plated contacts on clean copper were good for 40 amps per contact (we need 15). So in principle our sliding finger contacts (silver plated, of course) should be satisfactory. However there are two mechanical problems. The first is the alignment and concentricity problem of 15 ft. long pipes within pipes. We are cutting our moving annuli into 9 segments and with an arrangement of ceramic wheels and springs designing the fingers to have constant pressure contact force for out of roundness or out of concentricity of the stems and outer conductors of ± 1/8 inch. To insure that the stems are centered as well as they can be, we have adjusting screws to move the stems in three dimensions and a system involving telescopes and mirrors to look thru the ion source hole in the center of the machine to see that the position of each dee, and thus each stem, is correct. And thus, this problem is solved!

The second mechanical problem associated with the fingers is the possibility of galling, a process in which metal sliding on metal in vacuum without lubrication causes the surfaces to tear or gall. The amount of motion that can occur before galling becomes a problem obviously depends on which metals are rubbing against each other and on the smoothness or initial state of polish of each metal. We are presently undertaking tests in a cryogenically pumped vacuum environment to determine if silver on sandpapered copper will be satisfactory, or whether we will have to use more exotic techniques, such as electropolished gold or rhodium surfaces.

R.F. Transmitters

The transmitters will be 2 or 3 ft. diam. cans about 10 ft. high enclosing a 4CW50000E or 4CW100000E vacuum tube and a stub tuner which will be similar to the stem tuner. The final will be driven by a pair of 4CW2000 tetrodes using a lossy variable inductor between the driver anode and the final grid to simultaneously resonate the capacities and provide appropriate impedence transformation. The driver grids will be driven by a broad band untuned commercially available 50 watt amplifier.

Low Level Electronics

Figure 2 shows the overall plan for frequency, amplitude and phase control of the entire rf system. $\overline{F}$ stands for a frequency independent 90^{o} phase shifted signal. By appropriately adding F, $\overline{F}$, -F and $-\overline{F}$, one can obtain the $\pm 120^{o}$ phases. F+ stands for a single sideband of F, 2±.01 MHz higher in frequency. The purpose of F+ is to permit the phase detectors and limiting amplifiers to function at a constant 2 mHz by using a mixing and filtering process. This is the technique always used in synchrotrons, such as at PPA, FNAL, DESY, etc. This technique will also permit us to measure the phase of the extracted beam, even for 1nA beams where the pickup signal is buried in a sea of noise and rf pickup.

A conventional relay logic will provide personnel and high power equipment protection, but all display and low level interlock logic will be done with a dedicated minicomputer. This minicomputer will also be used to provide feedback control to the regulating loops, including the complete removal of any line frequency modulation of the dee rf voltages.

TABLE I.

Parameter	Units	18 Mhs	60 Mhz
STEM LENGTH			
Med. plane to short	Ft.	9	1.5
Power per dee	KW	50	50
rms current at short	Amps	1550	2100
Power density at short	W/in^2	15.5	49
Circulating energy	MVA	180	236
Equivalent cap/dee	pf	320	125
Shunt impedance/dee	ohms	$1.1x10^5$	$1.1x10^5$
Q	-	4000	5000
Drive capacitor	pf	4	1
Mode separation	ΔF/F	.0045	.012
Fine tuning capability	ΔF/F	.003	.008

FIG 1

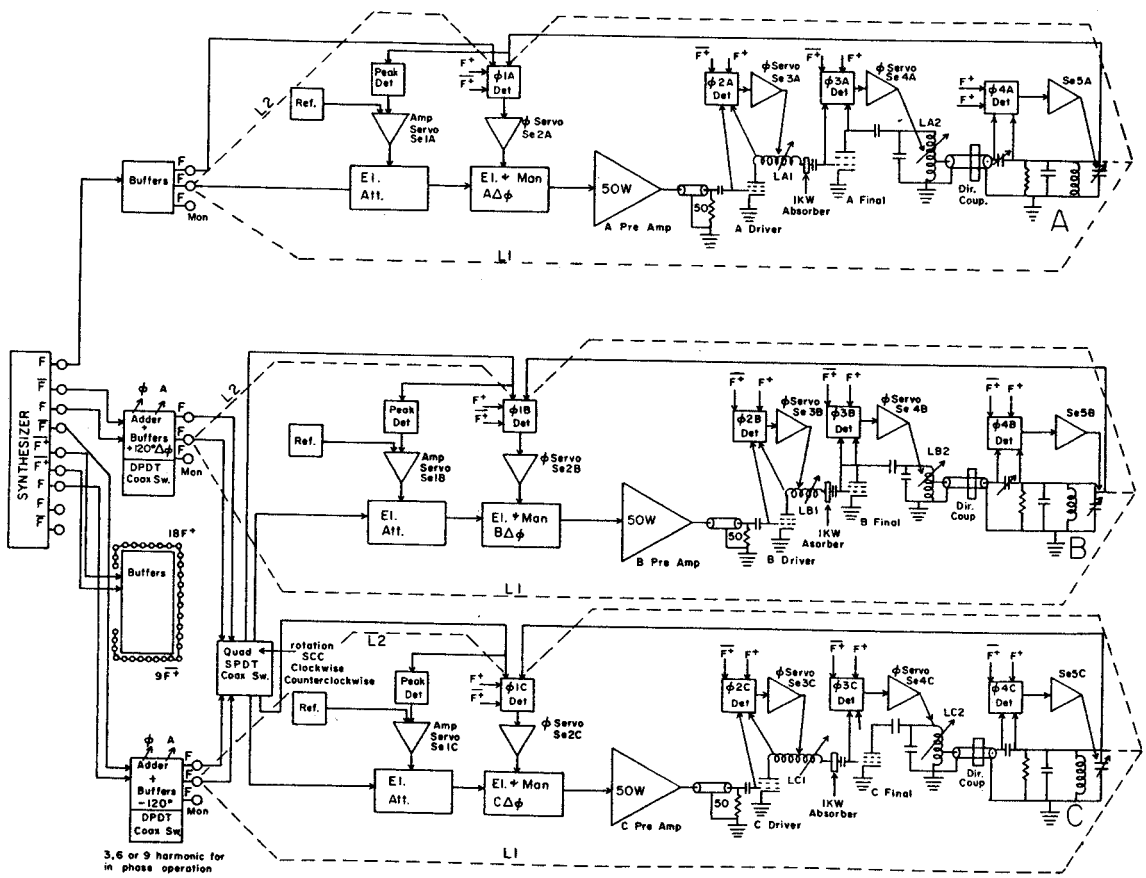

FIG 2

BLOCK DIAGRAM
MSU SUPERCONDUCTING CYCLOTRON
R.F. SYSTEM JUNE 30,1977

Further Studies of Beam Extraction for the 500 (q^2/A) MeV Superconducting Cyclotron

M.M. Gordon, C.J. Herrlander, and D.A. Johnson

The beam deflection system described in last year's progress report has been investigated more thoroughly and more extensively during the past year. The main results of these investigations are reported here and in the following two contributions. We restrict ourselves here mainly to a discussion of beam deflection by itself in order that a direct comparison can be made by the interested reader with the results presented in last year's report.

The current design for the deflection system still contains three electrostatic deflectors and three sets of focusing bars (F1, F2, F3) as indicated schematically in Fig. 1. The length and location of the electrostatic deflectors, as well as F1 and F2 are the same as those described in last year's report. However, the final set of focusing bars has been divided into six subsets (F3.1--F3.6) in order to provide more focusing power together with greater flexibility.

A detailed study of the complete field and field gradient produced by a set of focusing bars (as described in the next paper) has revealed certain added beneficial effects of these bars heretofore unrecognized For example, if the central ray moves down the center of the aperture, rather than along the line of zero field, we find that the region of linear focusing gradient is increased, and in addition, that the central ray moves along a line of negative field which then contributes significantly to the beam deflection process. Moreover, since this line occurs at a smaller machine radius than the line of zero field, the focusing bars can then be moved outward correspondingly thereby providing more clearance for inserting the bars. Fig. 2 shows a plot of the transverse gradient db/dx and the field decrease -b at the center of the aperture. The above mentioned advantages have allowed us to reduce the aperture in our revised design so as to achieve db/dx=7.7 kG/inch, rather than the 5 kG/inch reported last year. Also, the -b contribution of the focusing bars has enabled us to reduce the maximum field required from the electrostatic deflectors from the old value of 137.5 kV/cm down to 120 kV/cm in our present design. The focusing bars F1 and F2 have a=0.63 inch and a full height of 1.9 inch. The outer set F3,however, must be restricted to a maximum height of 1.4 inch in order to comfortably fit within the narrow gap between the upper and lower superconducting coils, and in order to maintain the same db/dx=7.7 kG/inch for these bars, their apertures have been reduced to a=0.58 inch.

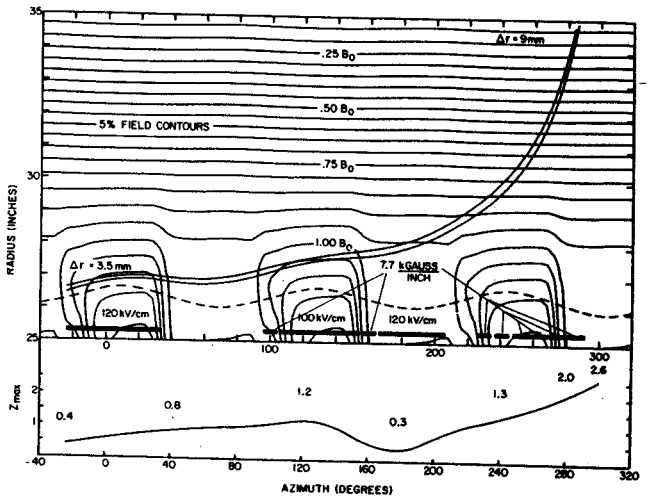

FIG. 1.--Plot of r(inch) versus θ(deg) for orbits of ions having E/A=49.3 MeV and Q/A=0.31 tracked through the beam deflection system presently under consideration. The two curves give the envelope of a set of orbits which start out at $\theta=-24^{\circ}$ on an emittance ellipse of 7.6 mm-mrad area and radial width of 3.5 mm. Shown in the background are the isogauss contour lines which range from $B=1.2B_0$ on the three hills near r=25 down to $B=0.15B_0$ near r=35, where B_0=47.4 kG. The ions pass through three electrostatic deflectors, the first ($\theta=-24^{\circ}$-$+32^{\circ}$) having 120 kV/cm strength, the second ($\theta=106^{\circ}$-154°) having 100 kV/cm strength, and the third ($\theta=166^{\circ}$-216°) having 120 kV/cm strength. As indicated, the ions pass through three sets of focusing bars (F1, F2, F3) with the third set divided into six subsets. Set F1 ($\theta=96^{\circ}$-102°) precedes the second deflector, the set F2 ($\theta=156^{\circ}$-164°) precedes the third deflector, and the final superset F3 is spread over a range from $\theta=226^{\circ}$ to $\theta=291^{\circ}$. Each set has a transverse gradient of 7.7 kG/inch and a reverse field -b=0.83 kG along the central ray of the beam. The beam passes through one dee in the first magnet valley, ($\theta=33^{\circ}$-93°) and runs outside the next dee in the second magnet valley, and finally emerges at $\theta=300^{\circ}$ (r=39) with a radial width of 9 mm (the figure has been cut off at r=35 here). The broken curve between r=26 and r=27 shows the periphery of the internal beam and thereby indicates the amount of clearance available for each element. Below the main part of the figure is a plot of z_{max} versus θ for a set of orbits performing linear vertical oscillations about the central ray during the deflection process. The units are arbitrary, and to provide a basis for judging the quality of the vertical focusing here, we should note that these same orbits have $z_{max}<3$ over the range E/A=40-49.3 MeV of their acceleration prior to deflection. As indicated here, $0.3<z_{max}<2.6$ ($\theta=300^{\circ}$) during deflection.

In order to emphasize how much the results shown in Fig. 1 here have improved, we should recall that the corresponding figure in last year's report showed the beam entering the deflection system with a radial width δr =2 mm and emerging at $\theta=300^{\circ}$ (r=35 inch) with δr =12 mm and emmittance of 6 mm-mrad. In the present case, the beam enters with a radial width of 3.5 mm and reaches r=35 inch at $\theta=285^{\circ}$ with δr =9 mm and an emmittance of 7.6 mm-mrad.

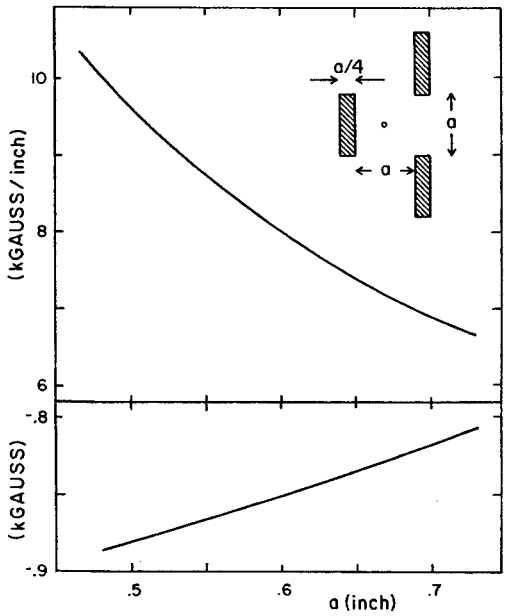

FIG. 2.--Plots of transverse gradient db/dx (at top) and field decrement -b (at bottom) at the geometric center of the focusing bar aperture as a function of the aperture size "a". The values of db/dx are given in kG/inch, and the values of -b are given in kG, over the range a=0.46 inch to a=0.72 inch. The inset shows a cross sectional view of the focusing bars defining "a" and showing the "center" of the aperture.

(Continuation from page 121 of article "Effects of Focusing Bars on Pre-extraction Orbits".)

The corresponding h=2 results shown at the bottom of Fig. 5 range from turn n=42 to turn n=58 where the final energy (49.3 MeV) is the same as the h=3 value. Here again, as in the h=3 case, we found that no added field bump was needed to generate adequate turn separation at the entrance to the first deflector. Indeed, this 0.14 inch turn separation is somewhat larger than the corresponding h=3 value (0.10 inch) noted above. Moreover, the h=2 results display none of the serious coupling effects between radial and longitudinal motion so evident in the h=3 case. Thus, on the final turn (n=58 here) the energy and phase spreads are 18 keV and 0.9°, while the (r,p_r) phase space area is practically the same as the initial value at 40 MeV. We therefore find that the h=2 results are superior in all respects to those obtained for h=3.

Compensation of the First Harmonic Field Component from the Focusing Bars

C.J. Herrlander, M.M. Gordon and D.A. Johnson

As reported in the annual report 1976 and in the previous contribution, the extraction system for the superconducting cyclotron is designed to consist of three electrostatic deflectors together with three sets of focusing bars, F1, F2 and F3, with the third set divided into six subsets (F3.1-F3.6). The locations of the different elements are indicated in Fig. 1. Each set or subset of focusing bars consists of three bars surrounding the beam in a geometry indicated in Fig. 2b. When exposed to a very strong, vertical magnetic field, the bars get saturated and generate a desired quadrupole focusing effect (cf. Figs. 2a and 2b).

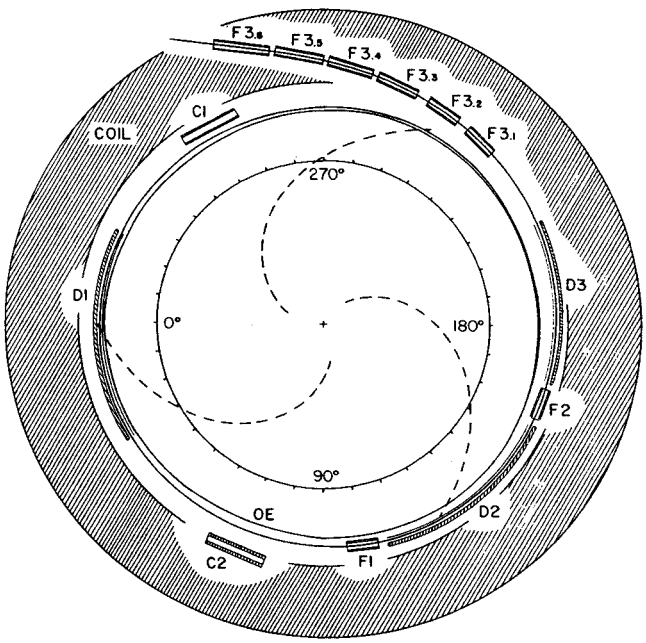

FIG. 1.--Schematic drawing of the 500 (q^2/A) MeV cyclotron showing the internal orbit envelope (OE) and an extracted ray having E/A=49.3 MeV and q/A=.31. The broken spiral curves indicate the center lines of the hills. The Fig. demonstrates the positions of the beam extraction elements consisting of three electrostatic deflectors (D1, D2 and D3) and three sets of focusing bars (F1, F2 and F3), the last one being split into six subsets. C1 and C2 indicate two sets of focusing bars introduced to cancel the first harmonic field component generated by the F1-3 sets. Azimuthal angles are indicated on a circle having a radius of 20 inches.

The addition of iron pieces disturbing the three sector symmetry of the magnetic field introduces orbit decentering effects which have to be cancelled. From orbit calculations it is found that the first harmonic component of the field has to be <<10 gauss at the ν_r=1 resonance radius, which for the field expected to be generated by the present magnet configuration is at 25.7 inches. The second harmonic component is expected to be about two orders of magnitude less important.

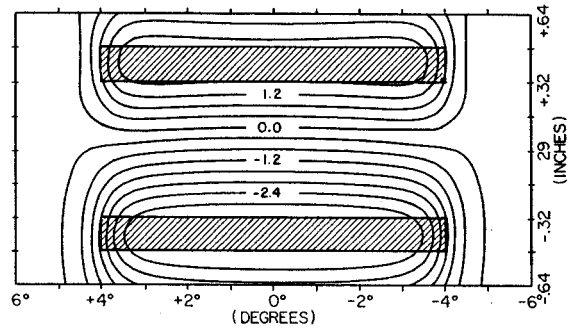

FIG. 2a.--Isogauss contour lines of the vertical field generated in the median plane by a set of focusing bars. The geometrical size of the set shown is close to the sets envisaged for the extraction system (a=.64 inch). Given field values are in KG.

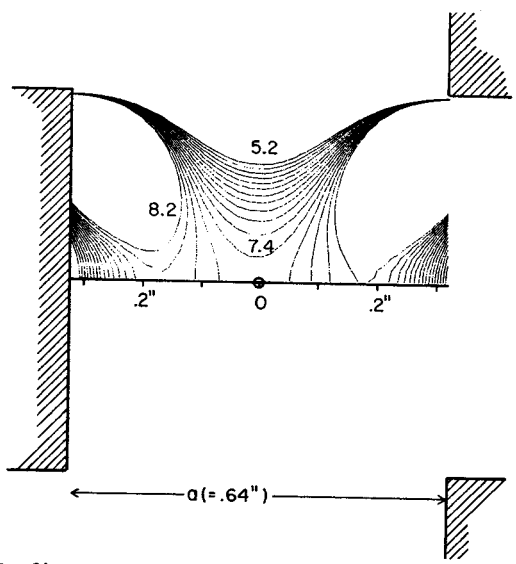

FIG. 2b.--Isogradient contour lines in an rz-plane through the center of the same set of focusing bars as in Fig.2a. The edges of the three bars are indicated as well as the beam position. Given gradient values are in kG/inch.

The first harmonic component of the disturbing field is more than two times stronger than the limit quoted. This field will be compensated by introducing sets of bars at such positions and of such sizes, that a complete cancellation of the first harmonic component at 25.7 inches is obtained. For simplicity it would be desirable to have a single compensating set. However, such a set would interfere with the first deflector, and therefore two compensating sets have to be introduced. Of these two sets (C1 and C2 in Fig. 1), C1 compensates for the first harmonic field component due to the two sets F1 and F2, whereas the other (C2) compensates for the field component from the third set F3 of focusing bars mentioned above. The different harmonic components resulting from the three sets of focusing bars plus the two sets of compensating bars are plotted in Fig. 3.

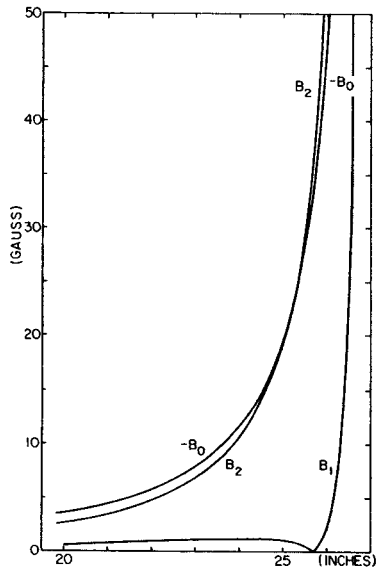

FIG. 3.--The average field B_0, and the amplitudes B_1 and B_2 of the first two harmonic field components generated by the three sets of focusing bars plus the two sets of compensation bars. The B_1 component is cancelled at r=25.7 inches where ν_r=1 for the unperturbed magnetic field. The fields are given in gauss, and note that $-B_0$ is plotted rather than B_0 itself.

Examination of the curves in Fig. 3 indicate a large value for $-(db_0/dr)$ in a radius region where it could provide a much needed increase in the vertical focusing. Using the formula: $\Delta(\nu_z)^2=-(R/B)(db_0/dr)$ to calculate the increase in ν_z values, we obtained the results shown in Fig. 4 for the total field (including the focusing bars). This figure also shows for comparison the corresponding ν_z values previously computed for the unperturbed field using the standard equilibrium orbit program. We see, for example, that at E/A=43.5 MeV where ν_z=0.054 has its minimum value in the unperturbed field, the total field value is ν_z=0.089, a rather significant improvement considering that the amplitude of the vertical oscillations generally varies as $(\nu_z)^{-\frac{1}{2}}$. Above about 45 MeV, the improvements in ν_z are relatively unimportant.

In addition to db_0/dr, the gradient db_2/dr contributes significantly to changes in the radial focusing frequency ν_r since this frequency is close to unity. Actual orbit computations show, for example, that the ν_r=1 resonance is shifted from 47.6 MeV in the unperturbed field down to 47.0 MeV in the total field. Moreover, between 47.6 and 49.3 MeV, the values of ν_r-1 for the total field are consistently lower than those for the unperturbed field, a result which should facilitate the precessional extraction process planned for this cyclotron. For example, at the nominal extraction energy 49.3 MeV, we find ν_r=0.66 for the total field, while ν_r=0.79 for the unperturbed field. See Fig. 5.

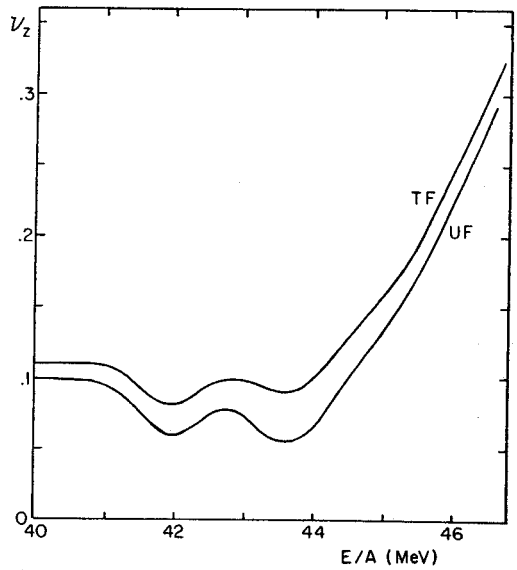

FIG. 4.--Vertical focusing frequency ν_z versus E/A between 40 and 47 MeV for the unperturbed field (UF) and for the total field (TF) including the focusing bars. Although the change at 43.5 MeV is rather significant, above about 45 MeV, the differences in the two curves become relatively unimportant.

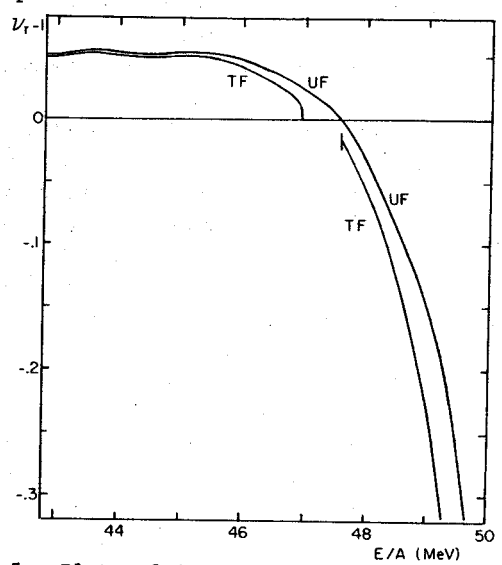

FIG.5.--Plots of (ν_r-1) versus E/A from 44 to 50 MeV for the unperturbed field (UF) and for the total field (TF) which shows the effect of the focusing bars. The UF curve is continuous, passing through zero at 47.6 MeV, and reaching -0.21 at 49.3 MeV, the nominal extraction energy. Below 47 MeV, the (r,p_r) phase space displays, in addition to the equilibrium orbit, three unstable plus three stable fixed points associated with the ν_r=3/3 nonlinear resonance. The field perturbations produced by the focusing bars cause (ν_r-1) to drop sharply to zero at 47.0 MeV, where the equilibrium orbit merges with one of the unstable fixed points so that both disappear at this energy. Between 47.0 and 47.6 MeV, the other two unstable fixed points pair off and annihilate with two of the stable fixed points. These processes result in the survival of only one stable fixed point above 47.6 MeV, which then assumes the role of the equilibrium orbit. Because of these complications, the TF curve shown above exhibits a break between 47.0 and 47.6 MeV. All these phenomena play an important role in the pre-extraction beam dynamics described in the following article.

Effects of Focusing Bars on Pre-extraction Orbits

M.M. Gordon, C.J. Herrlander, and D.A. Johnson

In order to induce turn separation at the entrance to the first electrostatic deflector, we plan to use the "precessional extraction" method which has proved so successful in our present machine and in many other isochronous cyclotrons. The basic procedure consists in accelerating the ions out beyond the isochronous region into the edge region of the magnetic field, thereby passing through the $\nu_r=1$ resonance where the addition of a carefully controlled **first harmonic** "field bump" drives the orbits off-center so that the resultant orbit precession produces the necessary large radius gain per turn at the deflector entrance. Considering the strong field gradients produced by the focusing bars in the crucial pre-extraction region $25<r<27$ (shown in Fig. 3 of the preceding article), we decided to investigate whether the effects of these gradients might interfere adversely with our standard beam extraction procedures. Our results so far, though admittedly quite tentative, indicate on the contrary that the focusing bars fringe fields provide assistance rather than hindrance to the precessional extraction performance.

Most of our results have been obtained for the third harmonic (h=3) mode of acceleration, since until quite recently the rf system was designed to operate only on this mode (and h=9). Now that a more general rf system is being designed, with h=1 and h=2 operation also possible, we shall present some preliminary results which indicate that as far as extraction is concerned, these modes are just as good as (if not better than) h=3.

All calculations reported on here were carried out with the "spiral gap" program which was designed specifically to include the effects of the radial as well as the azimuthal electric field in the gaps associated with spiral dees. As is appropriate for such an rf system, one "turn" corresponds to the ion returning to the same spiral gap line, rather than traversing 360° in θ. We have assumed that the three dees, located in the magnet valleys, have a constant angular width of 60° and a peak voltage of 100 kV independent of radius; the maximum voltage gain per turn is therefore (600 kV) sin (πh/6). With a nominal extraction energy of 49.3 MeV, all calculations were begun at 40 MeV where the magnetic field is still isochronous and the effects of the focusing bars are not yet noticeable.

Fig. 1 shows plots of the phase ϕ versus E/A obtained with h=1, h=2, and h=3 acceleration for "central ray" ions started on the equilibrium orbit in each case. The extraction energy, the final phase, and the total number of turns are: 49.3 MeV, 42°, and 51 turns for h=3; 49.3 MeV, 32°, and 58 turns for h=2; 48.7 MeV, 15°, and 94 turns for h=1. As expected, decreasing the h value here increases the total number of turns and decreases the final phase at extraction. Thus, the disadvantage of one effect is somewhat counterbalanced by the advantage of the other.

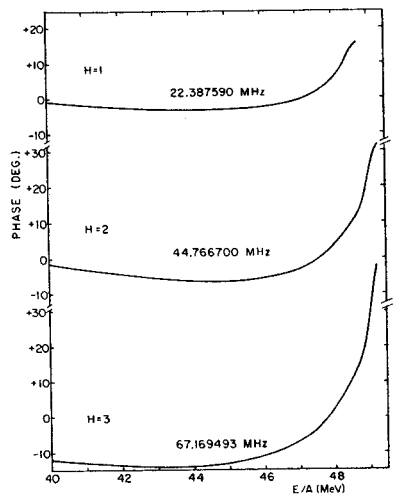

FIG. 1.--Plots of phase ϕ versus E/A in the pre-extraction region for first, second, and third harmonic (h=1,2,3) acceleration of ions having q/A=0.31 which all start on the equilibrium orbit at 40 MeV. The three quoted frequencies were adjusted to minimize the number of turns to the final extraction energy in each case. For the proposed dee system, the maximum voltage gain per turn is (600 kV)sin(πh/6).

Turning first to the h=3 results, Fig. 2 shows plots of p_x vs. x for the central ray orbit (whose phase-energy history is shown in Fig. 1) with points plotted once per turn along a fixed spiral line. Here, x and p_x denote the deviation of r and p_r from the instantaneous equilibrium orbit values. For purposes of contrast, the small inset shows the results obtained in the unperturbed field, and as can be seen, the accelerated orbit is never off center by more than 0.05 inch in this case. The main curve shows the corresponding results obtained with the total field (including the focusing bars) and here we find that the points are almost identical to those for the unperturbed field for the first 35 turns, but that the points then move off along a nearly straight line as the $\nu_r=1$ resonance is traversed, and that the points finally execute a large counterclockwise loop ending at x=0.28, $p_x=0.12$ on turn 51, where the orbit has its greatest off-centeredness (about 0.3 inch). We estimate that this off-centeredness could be effectively cancelled (if necessary) by an additional first harmonic field bump of strength 10-15 gauss, so that the effect of the

focusing bars is therefore not serious, at least in this respect.

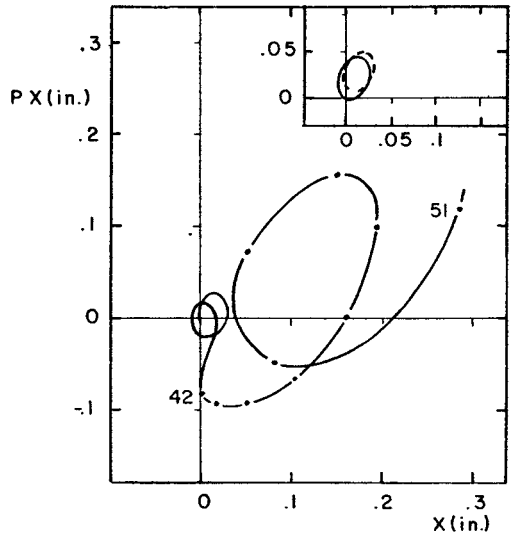

FIG. 2.--Plots of p_x versus x once per turn for the h=3 central ray orbit whose phase-energy curve is shown in Fig. 1 from 40 to 49.3 MeV. The small inset shows the corresponding results obtained for the unperturbed field (without focusing bars). Note that we convert all momenta into inch units through division by qB_o, where the field unit B_o=47.4 kG here.

To examine the effects on the radial motion more fully, an additional set of nine orbits was computed with exactly the same initial E and ϕ values as for the central ray, but with initial (r, p_r) values distributed around an eigen-ellipse centered on the central ray and having an initial radial width of 0.1 inch (about twice the radius gain per turn). The results of these calculations are displayed in a p_r vs. r phase space diagram given in Fig. 3 (top) which shows the evolution of this ellipse between turn n=39 (47.1 MeV) and the final turn n=51 (49.3 MeV). Here again, the points have been plotted once per turn along a fixed spiral line, but in this case the line was specifically chosen so that the final turn (51) occurs at the azimuth for the entrance to the first deflector. No added field bump was used here so that the most remarkable feature of these plots is the 0.1 inch clear radial separation between the last turn and all previous turns, thereby providing more than adequate clearance for the deflector septum. Not so evident perhaps, and somewhat disturbing, is the nonlinear deformation and actual twisting of the final "ellipse" which results from the coupling between the radial and longitudinal motion. That is, the nine orbits end up with an energy spread of 29 keV, a phase spread of 5°, and with an (r, p_r) area about one-half that of the initial ellipse at 40 MeV (see inset).

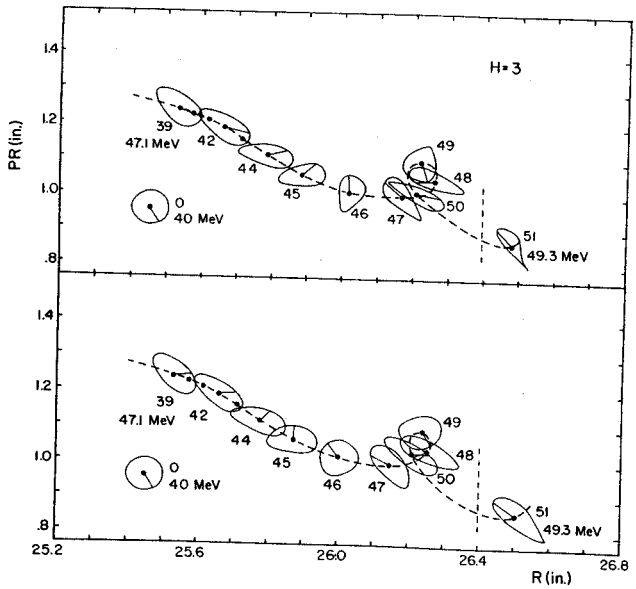

FIG. 3.--Phase space diagrams showing evolution of p_r versus r "ellipses" from turn n=39 (47.1 MeV) to the final turn n=51 (49.3 MeV) for h=3 acceleration. The inset shows the initial conditions at 40 MeV. The arrow indicates the displacement of one particular orbit from the central ray. The broken curve connects the points for the central ray plotted once per turn. To avoid confusion through overplotting, the ellipses are not shown on every turn until n=45. The diagram at top was obtained through normal acceleration as in Fig. 1 and Fig. 2, while the diagram at the bottom was obtained by artificially providing a constant energy gain at each dee gap crossing. The differences in these two diagrams therefore demonstrate the coupling effects between the radial and longitudinal motion.

For comparison, another set of orbits was computed with exactly the same initial conditions as those above, but with a constant energy gain at each dee gap crossing, thereby eliminating the coupling between the radial and longitudinal motion. This energy gain was specifically chosen to make the final central ray energy exactly the same as before. The corresponding results obtained for these ten orbits are shown at the bottom of Fig. 3 and as expected, although the resultant ellipses show some nonlinear distortion, the (r,p_r) areas remain invariant. Evidently, the nonlinear distortion (resulting from the ν_r=3/3 resonance) does not appear serious. We should note in passing that the ten points on the last (n=51) ellipse here provided the input data for the beam deflection calculation whose results are displayed in Fig. 1 of the article preceding the last one.

We have also studied the linear vertical oscillations associated with the h=3 accelerated orbits whose radial motion is represented at the top of Fig. 3. Of particular interest here, is the effect of the $\nu_r=2\nu_z$ coupling resonance which occurs at 47.9 MeV. Fig. 4 shows the evolution of five p_z vs. z phase space ellipses all of which start on exactly the same eigen-ellipse at 40 MeV as shown in the first panel. As can

be seen, the five ellipses remain practically indistinguishable up to n=39 (47.1 MeV), indicating negligible coupling effects up to this turn. The third panel for n=45 (48.2 MeV) demonstrates, however, that passage through the coupling resonance causes the five ellipses to fan out and to assume differing shapes. Evidently, these effects persist, but without further growth, up to the final turn n=51 (49.3 MeV). The net effect of the coupling resonance appears to be an overall increase in the axial phase space area occupied by the beam. However, since the value of z_{max} remains quite limited, no vertical beam loss should result. We should also note that the p_z vs. z ellipse shown here for the central ray for n=51 provided the input for the z_{max} calculation during beam deflection which is shown at the bottom of Fig. 1 in the paper preceding the last one.

We turn next to the results obtained for h=1 and h=2 acceleration with the central ray curves for ϕ vs. E/A again shown in Fig. 1. Here too we computed nine accelerated orbits in addition to the central ray with exactly the same (r,p_r) initial conditions at 40 MeV as those shown in Fig. 3 for h=3. The resultant p_r vs. r phase space diagrams are shown in Fig. 5, with the h=1 results at the top and the h=2 data at the bottom. For ease of comparison with Fig. 3, the r range (25.2-26.8) and p_r range (0.8-1.4) are exactly the same here.

Considering the first harmonic (h=1) results shown at the top of Fig. 5, it should be kept in mind that the energy gain per turn here is roughly half that for h=3, so that the turn numbers shown for a given energy are roughly twice those of Fig. 3. In order to improve the radius gain per turn on the final turn (n=94) at the deflector entrance, we found it necessary here to add a 10 gauss first harmonic field bump with a suitably chosen azimuth. Even so, the turn separation (0.04 inch) is significantly less here than in the h=3 case where no extra field bump was required. We found, however, that the h=1 orbits exhibited practically no coupling between the radial and longitudinal motion, with final energy and phase spreads of only 4keV and 1.3°. Although we have not yet tried it, the final radius gain per turn in the h=1 case might be increased significantly by accelerating the orbits still further so that the central ray executes one additional precession loop.

(Please turn to page 116 for final paragraph of this article).

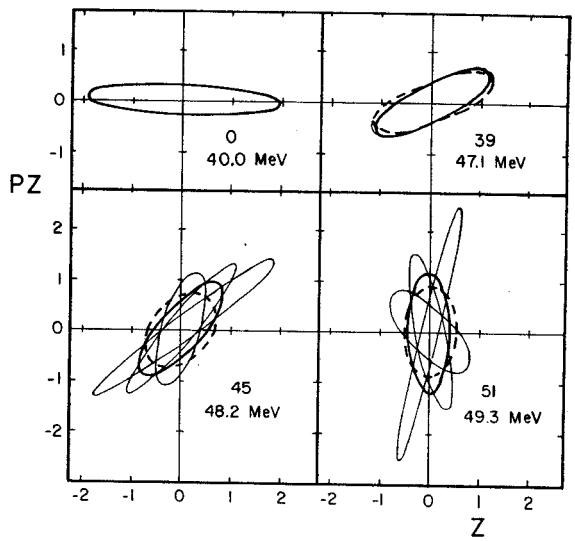

FIG. 4.--Evolution of the p_z vs. z ellipses characterizing the linear vertical oscillations about five of the ten accelerated orbits used to construct the radial phase space diagram at the top of Fig. 3. The heavy solid ellipse applies to the central ray, the broken line ellipse applies to the orbit indicated by the "arrow", while the other three ellipses here pertain to every other one of the remaining orbits in Fig. 3. The four panels here indicate results at 40 MeV (n=0), 47.1 MeV (n=39), 48.2 MeV (n=45), and the final energy 49.3 MeV (n=51). The changes in these figures clearly demonstrate the effects of the $\nu_r=2\nu_z$ coupling resonance which occurs at 47.9 MeV. Note that ν_z increases from 0.11 at 40 MeV to 0.53 at 48.2 MeV, and then to 0.81 at 49.3 MeV, which helps explain the changes in shape evident in these ellipses.

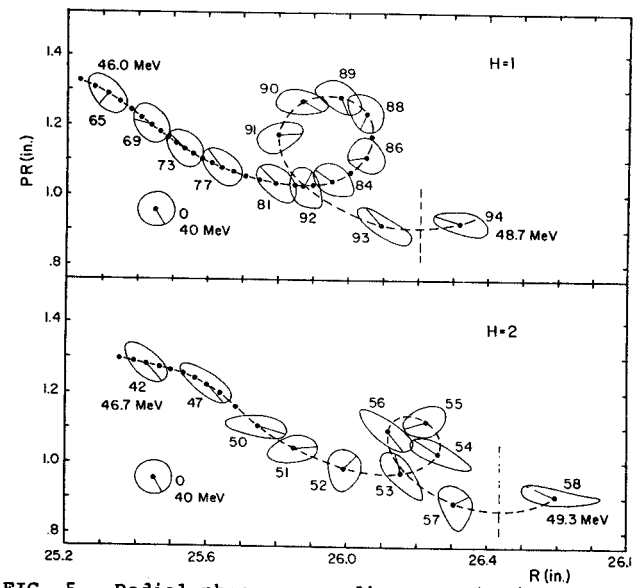

FIG. 5.--Radial phase space diagrams showing evolution of p_r vs. r "ellipses" obtained for first (h=1) and second (h=2) harmonic acceleration cases (cf. Fig. 1). The initial conditions at 40 MeV, the figure scales and other notations are identical to those used in Fig. 3 for the h=3 case. The h=1 diagram shown at top runs from n=65 (46.0 MeV) to n=94 (48.7 MeV), while the h=2 diagram shown at bottom runs from n=42 (46.7 MeV) to n=58 (49.3 MeV).